

LEO and LiMO Fuels: Structural and Rheological Characterization of Solvolytically Fractionated Lignin Dispersed in Alcohols

Saket Kumar, Jens Risbo, Jacob Judas Kain Kirkensgaard, and Yohanna Cabrera Orozco*

Cite This: <https://doi.org/10.1021/acssuschemeng.2c04017>

Read Online

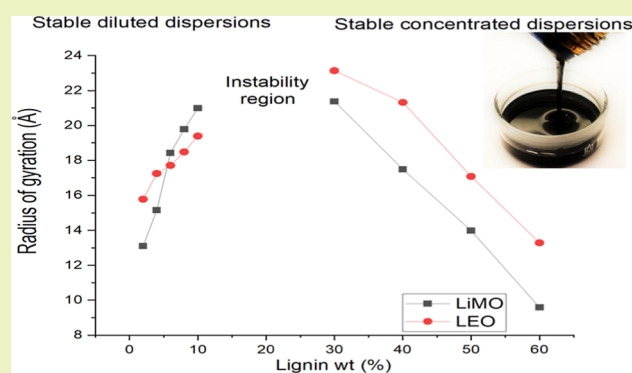
ACCESS |

Metrics & More

Article Recommendations

ABSTRACT: The mild thermal solvolysis of lignin in alcohols is a promising technology for obtaining carbon-neutral fuels. Incorporating lignin in ethanol and methanol leads to a rise in volumetric energy density in concentrated dispersions. The deployment of these fuels and their concentrated formulations depends on their structural and rheological properties. Here, we investigate mildly depolymerized Protobind 1000 lignin dispersed in ethanol (LEO) and methanol (LiMO) at different percentages of solids. Small-angle X-ray scattering (SAXS) data of diluted and concentrated LEO and LiMO dispersions show that, in these formulations, lignin exists in two states: individual lignin coil structures and their aggregates. The lignin coil structures are a few nanometers in size (3–5 nm) in both solvents. Direct observation of the lignin coil structures was achieved by cryo-TEM images and supports the findings of the SAXS measurements. The radius of gyration of the lignin coil structures in dilute dispersions increases with increasing lignin content, while in concentrated dispersions, the opposite trend is observed. It is hypothesized that in the concentrated regime, the lignin structures are more compressed by adjacent coils, resulting in the formation of a network-like arrangement. Furthermore, the aggregates of lignin coil structures can be detected by SAXS in the concentrated dispersions as they exhibit an upturn at low Q . Rheology measurements also indicate the presence of very fragile aggregate networks. The concentrated dispersions exhibit shear-thinning behavior in the shear rate range of 10^{-3} – 10^0 s^{-1} and Newtonian behavior at higher shear rates (10^0 – 10^3 s^{-1}). Moreover, the viscosities at high shear for ethanol and methanol samples are almost identical at the same solid percentages despite having slightly different water contents, suggesting that the interactions between lignin and the solvents do not determine the rheological behavior but rather the formation of the network structures formed by coils. Such polymeric networks are responsible for the stability of the dispersions at high solid percentages, while at low solid loads, the Brownian motion is sufficient to maintain the nanometer-sized lignin coils in the solvent.

KEYWORDS: ethanol–methanol fuel, lignin fuel, lignin dispersion stability, small-angle X-ray scattering, flow behavior



INTRODUCTION

The increasing concerns about the depletion of fossil fuels and their high carbon footprint have ignited the need to develop environmentally friendly, sustainable liquid fuels such as lignocellulosic biomass fuels. Lignocellulosic biomass mainly consists of 40–50% cellulose, 25–30% hemicellulose, and 15–20% lignin.¹ Global efforts in biorefinery research and development have gradually placed biofuels based on cellulose and hemicellulose, such as bioethanol, in the global energy market. Lignin, the second most abundant natural polymer, is still under-utilized in terms of making products of value. Most of the lignin produced by lignocellulosic biorefineries and paper-pulp industries is incinerated onsite to produce heat and power. The effective valorization of lignin plays a vital role in the economic sustainability of a lignocellulosic biorefinery and, thus, in the sustainable development of biofuels.

Lignin is a complex organic polymer composed of methoxylated phenylpropane units derived mainly from three monolignols: *p*-coumaryl alcohol (H unit), coniferyl alcohol (G unit), and sinapyl alcohol (S unit).^{2,3} Intensive research efforts have been invested toward lignin valorization for advanced biofuels. For this aim, approaches like lignin-first biorefining⁴ or reductive catalytic fractionation⁵ have gained momentum to develop fuels of energy content close to gasoline or diesel. Another approach is the mild thermolytic solvolysis of technical lignins in polar organic solvents to produce fuels of

Received: July 6, 2022

Revised: September 9, 2022

energy density close to that of ethanol or methanol, which can find application, for example, in the shipping industry.^{6–8} In mild thermolytic solvolysis, aqueous lignin-slurries (below 70% w/w water) or dried technical lignins are subjected to modified organosolv processes in methanol, ethanol, or other polar solvents under relatively mild reaction conditions (180–250 °C, 20 min to 1 h), and the process can be catalyzed or uncatalyzed for certain lignin types to increase yield.^{6–9} After solvolysis, two main fractions appear—a solid fraction and a liquid fraction—which have been characterized for Protobind 1000 lignin before.^{6–8}

Interestingly, the liquid fraction in ethanol and methanol solvents can be concentrated to reach a percentage of solids of 30, 40, 50, or even 60% while still being liquid at room temperature.^{7,8} This observation is important in the context of using ethanol or methanol as fuels, as alcohols have lower volumetric energy densities than conventional fuels. Adding more lignin into the solution increases the volumetric energy density proportionally.

Lignin structures in different solvents, that is, their morphology and molecular assembly, have been studied for other systems. For example, a recent study by Imel et al.¹⁰ reports the self-assembly of Kraft-processed softwood (SW) lignin, organosolv-extracted hardwood (HW) lignin, and acid-extracted lignin from wheat straw (WS) in polyethylene oxide (PEO). Authors report that adding PEO in SW and HW lignin solutions anisotropically directs the self-assembly of SW and HW lignins by increasing the length of cylindrical building blocks. Moreover, WS lignin forms swollen polymeric chain structures in solution, and their aggregate size non-monotonically increases with the addition of PEO. Various authors have reported that the lignin conformation and its aggregate size widely depend on the lignin source, extraction methods, and the dispersing medium.^{11–14} However, it is still unknown how the lignin assembles itself when dispersed in ethanol or methanol, and the factors affecting the shape, size, and conformation of lignin subunits have still not been studied in detail.

Likewise, the rheology of lignin dispersed in ethanol or methanol has been explored,⁸ but its relationship with the physical structure has not been discussed. Lignin rheology has been studied for other fuel systems, such as dispersions of acid-hydrophobized hydrolysis lignin in light crude oil, industrial oil, and diesel.¹⁵ The flow was described as Newtonian for dilute solutions with a transition to non-Newtonian with shear-thinning and thixotropy with increasing lignin concentration. It is unknown if, in alcohol systems, the same pattern is repeated. This information would be valuable for extensive fuel application studies, especially with high solid contents.

In this work, we used small-angle X-ray scattering, cryogenic transmission electron microscopy (cryo-TEM), and viscosity measurements to systematically investigate the structural and rheological behaviors of lignin in ethanol oil (LEO) and lignin in methanol oil (LiMO) with varying dry matter content to understand the potential of such dispersions in fuel applications. Additionally, the energy content of dispersion was measured as a function of dry matter content.

MATERIALS AND METHODS

Materials. Commercial Protobind 1000 alkali lignin was purchased from PLT Innovations, Switzerland. It has >90% sulfur-free lignin, < 3% hemicellulose, and <2% ash (minerals). The Protobind 1000 was used as received with no pretreatment or

modification. Lab-grade ethanol and methanol were purchased from VWR International, USA. The dry matter content of the lignin before sample preparation was 96%.

Sample Preparation. Solvolytically fractionated samples were prepared in methanol or 96% ethanol using a 1 L stirred Parr reactor at 200 °C and 18 bar. The reaction time was 20 min. Depending on the solvent, the solutions were named LEO (lignin ethanol oil) or LiMO (lignin methanol oil). The solid to liquid ratio was 1:5 w/w, and the stirring speed was 500 rpm. The solutions were filtered using the Büchner funnel with Whatman no. 4 filter paper (25 μm pore size). Subsequently, the solutions were concentrated to ca. 70% dry matter content using a Buchi Rotavapor R300 using a water bath at 50 °C. Then, the 60, 50, 40, and 30% solutions were diluted from the 70% solution. The percentages of lignin solubilized were 57 wt % for ethanol and 64% for methanol, in accordance with the values reported in the literature for Protobind 1000 lignin.^{6–8} Mass balances and chemical analysis of the derived fractions (solid and liquid) were reported in ref 6 to 8.^{6–8}

The dry matter content was determined on a heating plate at 105 °C for 10 min. Approximately 500 mg of LEO/LiMO was evenly distributed onto a 57 mm aluminum weight dish in triplicates. The dry matter content was determined as the weight of the wet mixture relative to the weight of the dried mixture.

Karl Fischer Titration. Volumetric water content determinations of LEO/LiMO dispersion with a dry matter content of 40% were performed on a Metrohm 870 KF Titrino plus using a connected oven at 200 °C. Hydranal CompositeS, the titration reagent, and methanol were used to carry out the reaction. Aliquots of 50–100 mg of LEO/LiMO were measured in triplicates.

Energy Density. The higher heating value (HHV) was measured in a 6400 oxygen bomb calorimeter (Parr Instrument Company, Parr, Illinois, USA). Cellulose tape (no. 610 from 3 M) was used for sealing potential openings to minimize sample evaporation. Benzoic acid pellets (Parr, Illinois, USA) were used as a reference. The density of the solution was measured by weighing 2.0 mL of the solution in Eppendorf tubes at 15 °C.

Sample Stability. Sample stability was analyzed as follows: for each sample, 10 to 20 ml of the aliquot was transferred to a 50 mL Falcon tube kept at 5 °C for 24 h. After refrigeration, the tube was heated to an ambient temperature and centrifuged at 765 g (rotor 1180 and 1000 rpm) for 10 min. A sample was considered stable when no sediment was present and unstable if a sediment was present in the test tube.

Small-Angle X-Ray Scattering (SAXS). SAXS measurements were performed with a Nano-inXider instrument from Xenocs. The instrument has a 40 μm-microfocus-sealed tube with a copper anode as the X-ray source, having a wavelength of $\lambda = 1.54 \text{ \AA}$. It operates at 50 kV and 0.6 mA for a total power of 30 W. In the instrument, two detectors with fixed positions were used to cover scattering wave vectors ($Q = 4\pi\sin\theta/\lambda$, where 2θ is the scattering angle) ranging from 0.0029 to 0.37 \AA^{-1} . The measurements were carried out in a very high-resolution configuration, allowing a 200 μm beam size on the sample with a typical flux of 4 Mph/s. 1.5 mm diameter glass capillaries with a wall thickness of 0.01 mm were used to load the samples. All SAXS measurements were carried out at 25 °C. Furthermore, data reduction was performed using the XSACT software to provide scattering curves of intensity as a function of the scattering vector. The Zimm plots were derived from the SAXS data of LEO and LiMO dispersions. All samples were measured 2 weeks after sample preparation to maintain consistency in the analysis.

Cryogenic Transmission Electron Microscopy (Cryo-TEM). Imaging of diluted 2 wt % LEO and LiMO samples was performed using a transmission electron microscope (JEM-2200FS) equipped with a 200 kV field-emission electron source. It has an in-column energy filter (Omega filter) which eliminates the inelastic electrons, resulting in high-contrast, clear images. 20 μL samples were first placed on the copper TEM grid, and the extra samples were bloated out; then, the sample-loaded grid was dipped into liquid nitrogen to vitrify the samples. Moreover, the captured cryo-TEM images are converted to 8-bit images, and the scales were appropriately set. The

particle size distributions of lignin in LEO and LiMO dispersions were determined using the Image J software.

Rheology. Rheological measurements were carried out with a Discovery Hybrid Rheometer (HR - 30, TA Instruments). TRIOS software was used to control the rheometer. A concentric cylinder geometry consisting of cup and bob, with a diameter of 30.37 mm and 27.99, respectively, was used. A TA instrument solvent trap was used to prevent sample loss from evaporation during measurements. The shear flow experiments were conducted at shear rates of 10^{-3} – 10^3 s^{-1} at a constant temperature of 25 °C. The samples were equilibrated for 900 s before starting the measurements. Ten data points were collected per decade.

RESULTS AND DISCUSSION

Results. Energy Density and Water Content. The gravimetric and volumetric energy densities of the LEO and LiMO dispersions were estimated based on a higher heating value (HHV). Table 1 lists the energy density values for LEO and LiMO dispersions at different lignin dry matter contents.

Table 1. Measured Energy Density Values for LEO and LiMO Dispersions

	dry matter %	gravimetric energy density (HHV)		density (mg/mL)	volumetric energy density MJ/L
		MJ/Kg	(s.d)		
95% methanol	0	19		0.8	15
LiMO	30	23.7	(0.1)	0.83	20
LiMO	40	24.1	(0.0)	0.89	21
LiMO	50	24.5	(0.1)	0.94	23
LiMO	60	24.6	(0.3)	0.96	24
95% ethanol	0	27		0.8	22
LEO	30	26.9	n.a	0.83	22
LEO	40	27.1	(0.0)	0.89	24
LEO	50	27.2	(0.1)	0.94	26

Kouris and colleagues⁶ reported similar values of 29.7 and 30.3 GJ per ton for similar solutions based on ethanol and methanol with unspecified lignin dry matter content. Here, we show that due to increased density, the volumetric energy density is increased with increasing lignin concentrations.

The water contents of the dispersions with 40% dry matter were 7.2% (s.d = 0.27) for LEO and 3.3% (s.d = 0.26) for LiMO. Slight differences in water content between ethanol dispersions of varying dry matter contents are expected, as 96%-ethanol contains water. The water in the methanol dispersions came from lignin and the evaporation process, as water molecules seem to be concentrated. These slight differences in water content among dispersions are a caveat that has to be considered when interpreting the final results. However, it is important to note that despite having slightly different water contents, ethanol solutions still have a higher HHV than methanol dispersions and that the increase in HHV with increasing lignin concentration is consistent between both solvents, suggesting that the difference in water content can be negligible.

Stability Analysis. The solubilized lignin and its concentrated dispersion behave similarly to colloidal suspensions in the sense that they are a two-component system in which the elements of the dispersed phase are too small to be observed with an optical microscope, and their movement is affected by thermal forces.¹⁶ In addition, the stability of the dispersions at

5 °C changes with an increase in concentration, as reported before.⁷ Figure 1 shows that both dilute (≤ 10 wt % lignin) and

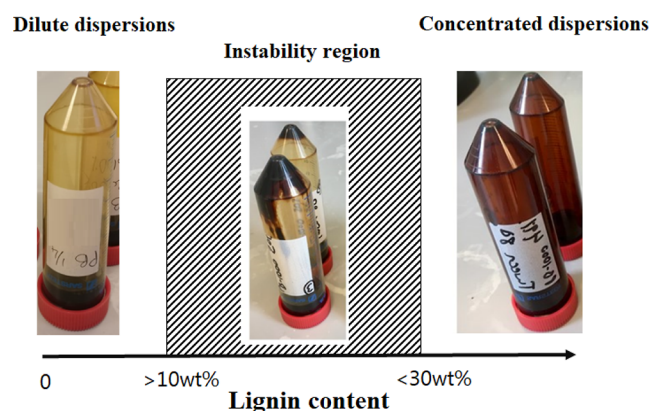


Figure 1. Stability of the LEO and LiMO dispersions as a function of lignin content.

concentrated (≥ 30 wt % lignin) samples do not phase-separate when cooled to 5 °C and centrifuged, but the instability region samples between 10 wt % and 30 wt % have precipitated lignin stuck at the bottom of the inverted Falcon tube.

SAXS. Dilute Dispersions. Figure 2a,c shows the small-angle X-ray scattering data for LEO (2 a) and LiMO (2 c) dispersions with varying dry matter contents (2 to 10 wt %). Figure 2b,d is obtained by plotting $I(Q) \times Q^2$ vs Q , commonly known as Kratky plots. The Kratky plots divide out the decay of the scattering, making other features more evident. This analysis is often used on polymeric dispersions to identify the conformation of the polymeric chains.¹⁶ In such a representation, a pseudo-linear rise in the plot would suggest a rod-like conformation, a rise to a plateau suggests a random coil conformation, and a distinct peak or a bell shape represents a compact globular shape.^{17,18} The Kratky plots, Figure 2b,d, show the typical scattering pattern from random coils, seen as a rise to a plateau at high Q values. Moreover, the Kratky plot of LiMO dispersions indicates a slightly more compact polymeric configuration than LEO dispersions. The scattering data were further analyzed using the mono Gaussian coil model, as during sample preparation, we separated the large molecular weight long polymeric chains with filtration.⁹

Mono Gaussian Coil Model. This model describes the scattering from the monodisperse polymeric chains in solvents or polymer melts.

The monodisperse Gaussian coil is of the form:¹⁹

$$I(Q) = \text{Scale} \times I_0 \times P(Q) + \text{Background} \quad (1)$$

$$I_0 = \phi_{\text{poly}} \times V \times (\rho_{\text{poly}} - \rho_{\text{solv}})^2 \quad (2)$$

$$P(Q) = 2[\exp(-(QR_g)^2) + (QR_g)^2 - 1]/(QR_g)^4 \quad (3)$$

$$V = M/(N_A \delta) \quad (4)$$

where I_0 is zero Q intensity, and $P(Q)$ is a single-chain form factor. ϕ_{poly} and ρ_{poly} are the volume fraction and scattering length density (SLD) of polymeric chains, respectively. ρ_{solv} is the SLD of the solvent, V is the volume of polymeric chains, R_g is the 18 of the polymer chain, M is the molecular weight of the polymer, N_A is the Avogadro's number, and δ is the bulk

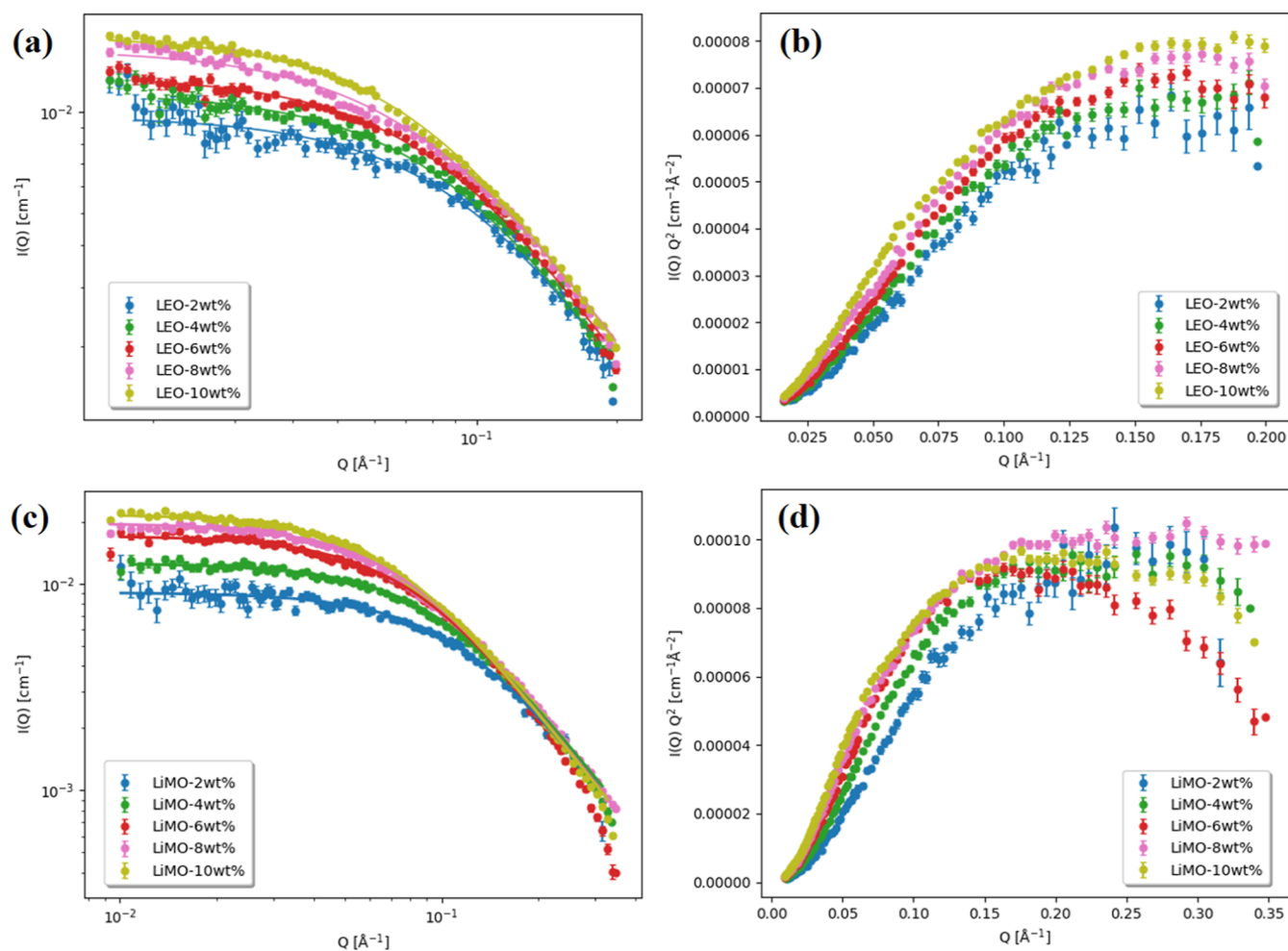


Figure 2. (a,c) Small-angle X-ray scattering profiles of LEO and LiMO samples at different dry matter percentages and associated model fits. (b,d) Standard Kratky plots for LEO and LiMO, respectively.

density of the polymer. The background is the incoherent scattering and noise contribution.

The fitting results of the mono Gaussian coil model suggest that the radius of gyration of the lignin coil structure in LEO and LiMO dispersions increases with increasing the lignin dry matter content from 2 to 10 wt %, with no apparent differences between the two solvents (Table 2). χ^2 is the fitting error of the used model to match the experimental data. Assuming the lignin coil structure as a spherical particle, the R_g can be approximated to the particle radius (R) as $R_g = R \times \sqrt{3/5}$.

Table 2. Results of SAXS Data Analysis Using the Mono Gaussian Coil Model

	R_g (Å)	I_0 (cm ⁻¹)	χ^2
LEO-2wt %	15.78	0.009	1.4
LEO-4wt %	17.25	0.0114	2.53
LEO-6wt %	17.71	0.012	2.22
LEO-8wt %	18.48	0.015	5.98
LEO-10 wt %	19.69	0.016	3.53
LiMO-2wt %	13.1	0.009	0.99
LiMO-4wt %	15.16	0.012	3.17
LiMO-6wt %	18.42	0.017	8.24
LiMO-8wt %	19.78	0.019	7.23
LiMO-10 wt %	20.98	0.022	5.5

From Table 2, LiMO-10 wt % has the highest radius of gyration value, and for this, the corresponding particle radius is 2.71 nm.

The weight-average molecular weight for the lignin dispersed in ethanol and methanol was determined by Zimm analysis.²⁰ In the low Q and low concentration regime, the scattering intensity from lignin in ethanol and methanol can be approximated as:²¹

$$\frac{Kc}{I} = \frac{1}{M_w} \left(1 + \frac{R_{g,0}^2 Q^2}{3} \right) + 2A_2c \quad (5)$$

where

$$K = \frac{\Delta\rho^2}{N_A d_{\text{lignin}}^2} \quad (6)$$

K is the contrast factor, c is the lignin concentration, I is the scattering intensity, M_w is the weighted average molecular weight, $R_{g,0}$ is the radius of gyration of lignin at infinite dilution, A_2 is the second virial coefficient, $\Delta\rho$ is the scattering length density difference between the lignin and the solvent used, and d_{lignin} is the solid-form lignin bulk density (1.35 g/mL).^{21,22}

Figure 3 shows the typical Zimm plot, where Kc/I versus Q^2 is plotted. The scattering data of four different concentrations

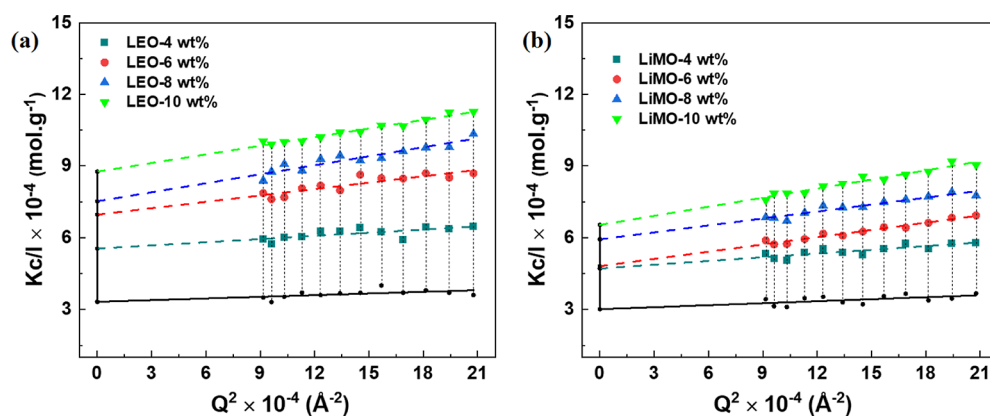


Figure 3. Zimm plot for (a) LEO and (b) LiMO dispersions. The dashed line represents the linear fits extrapolated to zero concentration and Q tending to zero (black solid circles).

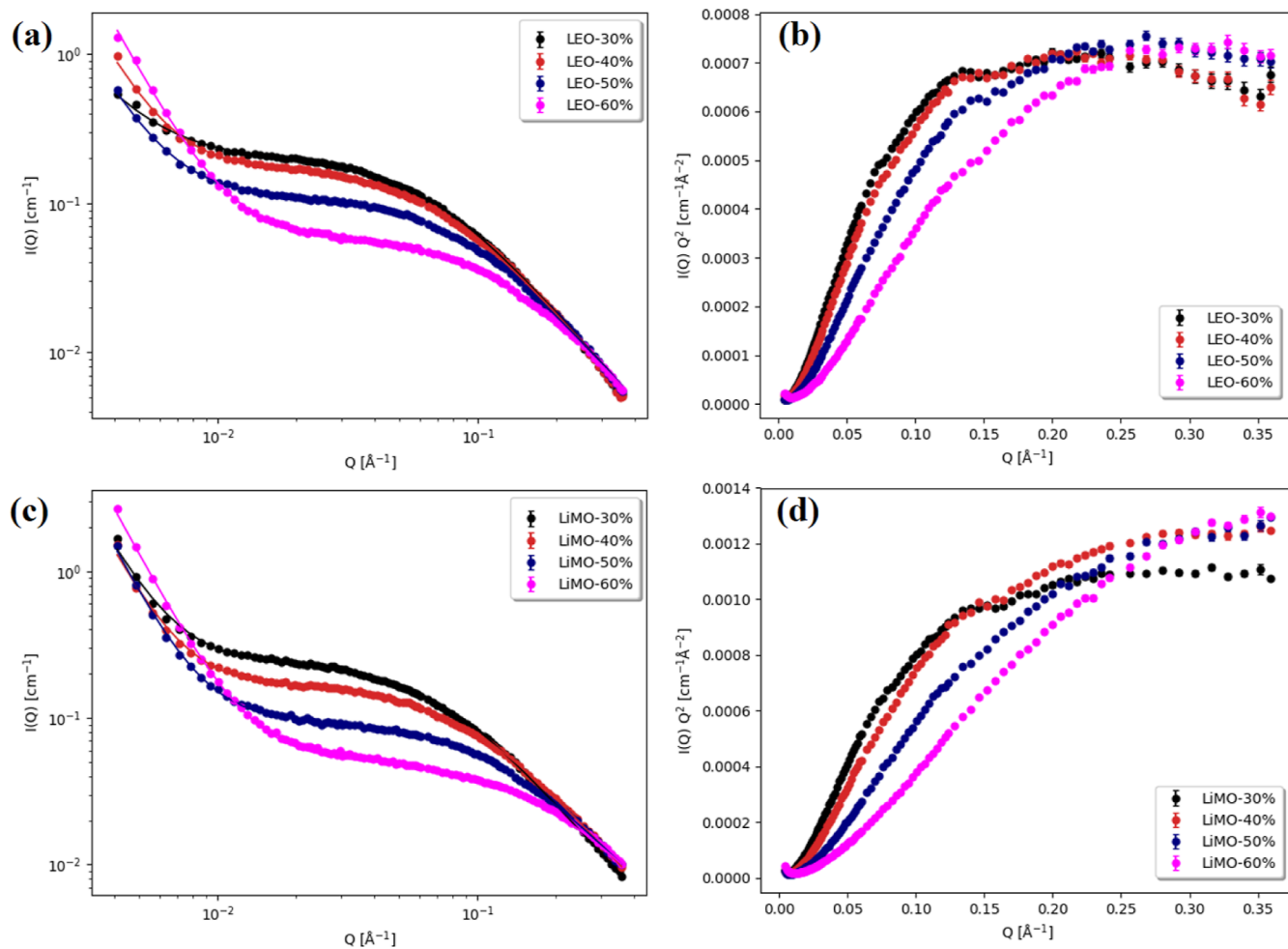


Figure 4. (a,c) SAXS profiles of concentrated LEO and LiMO dispersions at different dry matter contents. The solid line represents the combined power law and mono Gaussian coil model fitting. (b,d) Standard Kratky plots.

of LEO- 4, 6, 8, and 10 wt % are used. The Zimm plot was constructed in the Q range of $0.03\text{--}0.045\text{ \AA}^{-1}$, as this region has low noise data and satisfies the low Q and low concentration criteria ($QR_g < 1$). On extrapolating the Kc/I data to Q and c equal to 0, the lignin molecular weight is obtained. The analysis suggests that the weighted average molecular weight of the Protobind 1000 lignin fractions is 3030.3 Da and 3333.3 Da for LEO and LiMO suspensions, respectively, suggesting that the solvent determines the molar

mass distribution of the extracted fractions in solution, in accordance with data published by Kouris and colleagues.⁶

Concentrated Dispersions. The SAXS profile for concentrated LEO and LiMO dispersions for lignin dry matter contents varying in the range of 30–60 wt % is shown in Figure 4 (a and c, respectively). Both the concentrated LEO and LiMO samples exhibit up-turns at low Q ($<10^{-2}\text{ \AA}^{-1}$), indicative of the aggregation of the smallest structural units (referred to as lignin coil structures). The scattering profiles

Table 3. Results of SAXS Data Analysis Using the Combination of Power Law and Mono Gaussian Coil Models

sample	scale _{coil}	$I_{0,coil}$ (cm ⁻¹)	R_g coil (Å)	scale _{power}	slope _{power}	poly-dispersity in R_g	χ^2
LEO-30%	1.14	0.21	23.14	3.53×10^{-6}	2.11	0.18	2.96
LEO-40%	0.005	32.64	21.32	5.11×10^{-8}	2.98	0.19	3.87
LEO-50%	36.73	0.002	17.08	1.48×10^{-7}	2.68	0.24	3.01
LEO-60%	17.78	0.001	13.29	8.65×10^{-9}	3.22	0.25	7.5
LiMO-30%	1.23	0.22	21.389	2.03×10^{-8}	3.28	0.14	18.39
LiMO-40%	0.022	1.02	17.497	9.59	3.44	0.22	14.74
LiMO-50%	0.18	0.069	13.997	7.6	3.49	0.31	3.12
LiMO-60%	0.12	0.108	9.588	8.2×10^{-9}	3.30	0.31	7.48

suggest that the concentrated LEO and LiMO dispersions contain two structural levels: the smallest structural unit and the aggregates. Due to the instrument limit and limited available data points at low Q , the size of the aggregates cannot be determined. At mid- Q , the scattering intensity of concentrated LEO and LiMO dispersions decreases with increasing the dry matter content, suggesting a decrease in the size of the lignin coil structures. Furthermore, at high Q , all the scattering profiles coincide to form a single curve, indicating that the structure of the smallest lignin structural units is the same.

Figures 4b,d shows the standard Kratky plots for concentrated LEO and LiMO dispersions. These Kratky plots exhibit the typical scattering pattern from random coils, like dilute dispersions (Figure 2). The two structural levels of the SAXS profile are analyzed using the power law model for the low Q regime and the mono Gaussian coil model for the intermediate to high Q regime. The combined power law and mono Gaussian coil models are discussed in the next section.

Combined Power Law and Mono Gaussian Coil Models. The small-angle X-ray scattering data are analyzed by combining a power law and a mono Gaussian function. The power law model describes the low Q region of the scattered intensity data, representing larger aggregates with sizes beyond the resolution of the available Q -range. The mono Gaussian coil describes the mid- Q to high- Q region, describing the local biopolymer structure.

The combined power law and mono Gaussian coil is of the form:^{19,23}

$$I(Q) = \text{Scale} \times (\text{Scale}_{\text{power}} \times Q^{-n} + \text{Scale}_{\text{coil}} \times I_0 \times P(Q)) + \text{Background} \quad (7)$$

where n is the power-law exponent. The solid line in Figure 4a,c is the model fitting of the experimental data. Table 3 lists the fitting results of the combined power law and mono Gaussian coil models.

The power law exponent ranges between 2 and 3.5, suggestive of the mass fractal nature of the lignin in the concentrated LEO and LiMO dispersions. The radius of gyration decreases with increasing the dry matter content, suggesting that the lignin coil structures get compressed by increasing the dry matter content (Figure 5).

Cryo-TEM. Cryo-TEM images of 2 wt % LEO and LiMO are shown in Figure 6a,b, respectively. The area having the maximum number of lignin coil structures in the image is chosen, and subsequently, the size of around 100 particles is measured manually in the ImageJ software. Our analysis confirms that the size (diameter) of lignin in LEO and LiMO dispersions is ~ 3 and ~ 3 –5 nm, respectively (Figure 6c,d).

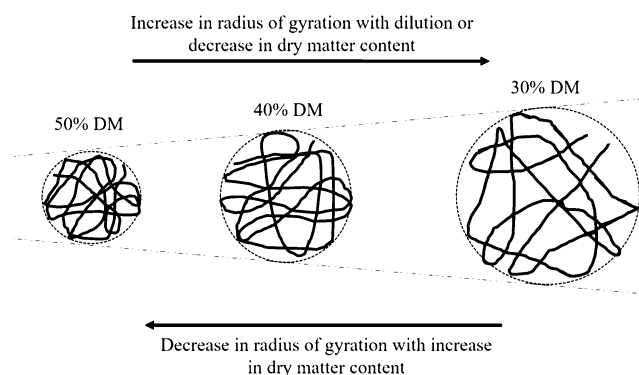


Figure 5. Schematics for the effect of an increase in dry matter content and dilution on the radius of gyration of lignin coil structures in concentrated LEO and LiMO dispersions.

The observed lignin diameter is qualitatively in agreement with the radius of gyration predicted by the SAXS measurement.

Rheology. Figure 7a,b shows the flow curve measurements of the concentrated LEO and LiMO dispersions, respectively, in the shear rate range of $\sim 10^{-3}$ – 10^3 s⁻¹. No data were recorded for LEO-30% in the shear rate of $\sim 10^{-3}$ s⁻¹, as the sample does not exhibit sufficient torque at these shear rates. The viscosity of both LEO and LiMO dispersions increases with increasing lignin dry matter content. Both the LEO and LiMO dispersions have approximately the same viscosity at a given lignin dry matter content at high shear rates. The LiMO dispersions exhibit relatively higher viscosity than LEO's at a low shear rate. The flow curve measurements exhibit prominent shear-thinning behavior in the low shear rate range (< 1 s⁻¹). On further shearing above 1 s⁻¹, both the LEO and LiMO dispersions show the characteristics of Newtonian fluid as the viscosity remains almost constant with respect to the shear rate. The results suggest that low shearing of ~ 1 s⁻¹ is sufficient to break the network of aggregated lignin coil structures, and these structures get aligned in the direction of shear. Therefore, it can be concluded that the small structural units of Protobind 1000 lignin form very fragile networks in ethanol and methanol, which can easily be disturbed by minimal shearing.

The viscosity versus shear rate data are modeled using the Sisko model, as they are applicable for both the shear-thinning and the constant viscosity regime. Sisko model is applied in the full shear rate range of 10^{-3} – 10^3 s⁻¹ for LEO and in the range of $\sim 10^{-2}$ – 10^3 s⁻¹ for LiMO dispersions.

$$\text{Sisko model: } \eta = \eta_{\infty} + K\dot{\gamma}^{n-1} \quad (8)$$

Here, η is the shear viscosity, $\dot{\gamma}$ is the shear rate, K is the fluid consistency index, and n is the flow behavior or power law index. When $n = 1$, the fluid is Newtonian; when $n < 1$, the

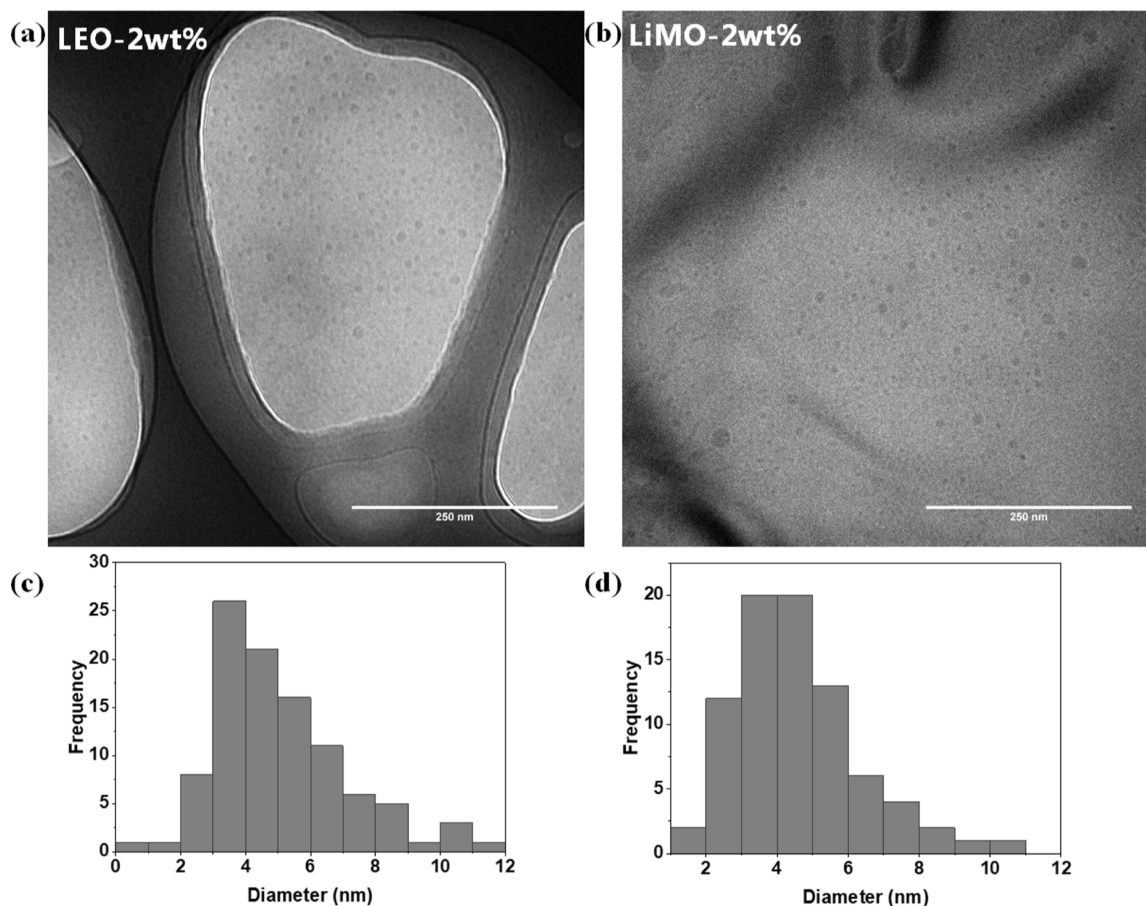


Figure 6. (a,b) Cryo-TEM images of 2 wt % LEO and LiMO suspensions, respectively, and (c,d) shows their particle size distribution.

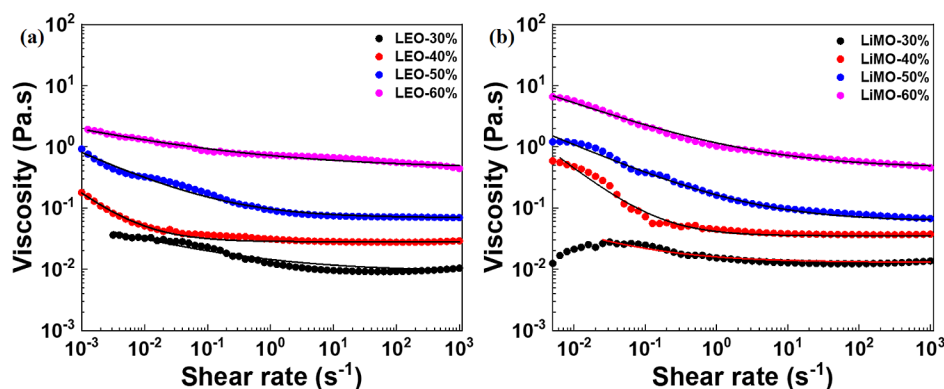


Figure 7. Viscosity vs shear rate for different dry matter percentages of (a) LEO and (b) LiMO. The solid line represents the Sisko model fits.

fluid is shear thinning; and when $n > 1$, the fluid is shear-thickening. The fact that $R^2 > 0.94$ in all dispersions (Table 4) suggests that the Sisko model accurately describes the rheometry.

DISCUSSION

The lignin-content-dependent stability of the dispersions can be explained using the schematic illustration shown in Figure 8. In dilute dispersions, the small structural units formed by polymeric lignin coils remain randomly dispersed, and their size is so small that the Brownian motion overcomes the gravitational force, as reported for other systems.¹⁵ Brownian forces acting on a colloidal particle arise from the random thermal collisions of the suspending medium molecules. It can

Table 4. Results of Sisko Model Fitting

sample	η_{∞}	K	n	R^2
LEO-30%	0.009	0.005	0.69	0.95
LEO-40%	0.028	0.0005	0.19	0.99
LEO-50%	0.069	0.027	0.52	0.98
LEO-60%	0.440	0.281	0.75	0.99
LiMO-30%	0.013	0.003	0.52	0.94
LiMO-40%	0.035	0.006	0.09	0.96
LiMO-50%	0.061	0.102	0.50	0.97
LiMO-60%	0.450	0.706	0.58	0.99

be defined in terms of thermal energy as Brownian force $F^B = k_B T/a$, where k_B is the Boltzmann's constant ($1.381 \times$

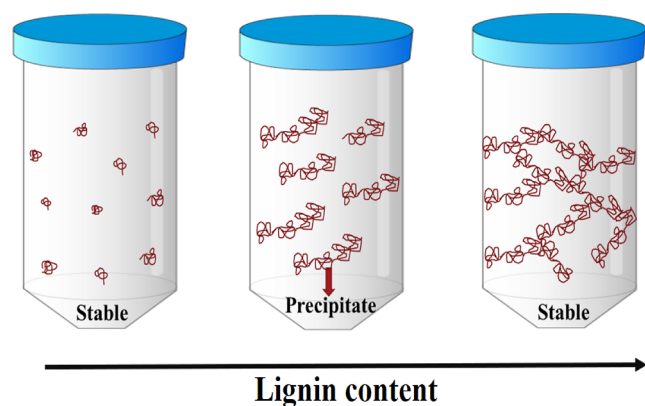


Figure 8. Schematic for lignin-content-dependent stability of the LEO and LiMO dispersions.

$10^{-23} \text{ J K}^{-1}$), T is the absolute temperature, and a is the particle radius. Furthermore, according to the Archimedes principle, the force of gravity F^g acting on a spherical colloidal particle of density ρ_p in a suspending medium of density ρ_m is given as, $F^g = (\rho_p - \rho_m) \frac{4}{3} \pi a^3 g$. When the Brownian force is smaller than the force of gravity, the suspended particle will precipitate (or cream if the particle density is lower than the suspending medium). It is reported that, for colloidal-sized particles, the Brownian force is often comparable to or more than that of the gravitational force.²⁴ Here, the F^B for tiny lignin coil structures, even at a low temperature of 5°C , is around $1.4 \times 10^{-12} \text{ N}$, which is significantly higher than the F^g which is around $4.6 \times 10^{-22} \text{ N}$, better explaining the reason for stable dispersions. It is noteworthy that F^B scales with a^3 and F^g scales linearly with a , so the F^B will be the dominant force for larger particles.

In the instability region, the dispersed lignin coil structures may interact with the adjacent lignin coil structures and form larger clusters or aggregates, leading to precipitation under gravity. Moreover, in the concentrated regime, the aggregates of lignin coil structures might form an interconnected network, preventing the precipitation of lignin from the dispersing medium.²⁵ The formation of the spanning network is accompanied by the phenomena of shear thinning (cf. Figure 7), showing that the formed networks are fragile and can be taken apart even at low shear.

Furthermore, from Tables 2 and 3, the effect of dry matter content on the radius of gyration of lignin coil structures in both dilute and concentrated regimes is shown in Figure 9. In the dilute regime, the radius of gyration of lignin coil structures increases with increasing the dry matter content, and in the concentrated regime, the opposite trend is observed. This suggests that in a dilute regime, lignin coil structure size increases with increasing the lignin concentration; and in the concentrated regime, the lignin coil structures get compressed by adjacent lignin coils. The increase in the size of the lignin structural units in the diluted region suggests that they do not consist of single lignin polymers, but on average, more lignin materials are added to the structural units when increasing the concentration until the instability limit is reached.

CONCLUSIONS

A combination of analytical techniques was applied to investigate the structure of solvolytically fractionated Proto-bind 1000 lignin in dispersions of ethanol (LEO) and

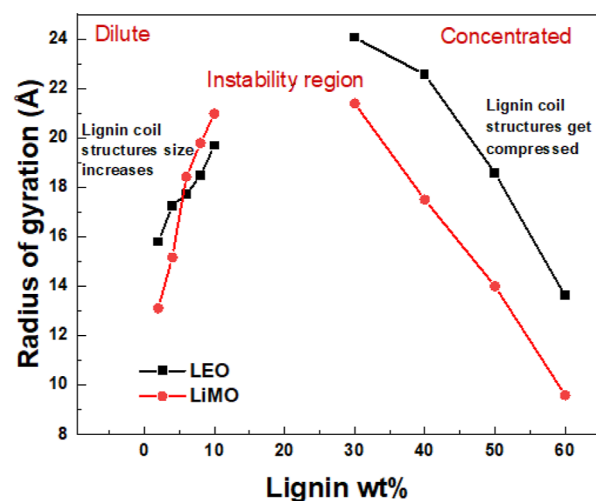


Figure 9. Radius of gyration versus lignin wt % for dilute and concentrated dispersions.

methanol (LiMO) at different percentages of solids. The SAXS data of dilute and concentrated LEO and LiMO dispersions show that the lignin coil structures are few nanometers in size (3–5 nm) in ethanol and methanol solvents. Direct observation of the lignin coil structure was achieved by cryo-TEM images and supports the findings of the SAXS measurements. The radius of gyration of the dilute dispersions increases with increasing the lignin content, while in the concentrated dispersions, the opposite trend is observed. It is hypothesized that in the concentrated regime, the lignin coils get more compressed by adjacent coils. The concentrated dispersions exhibit an upturn at low Q , indicative of aggregation of lignin coil structures. The network of these aggregates leads to the stability of the concentrated dispersions. These networks are very fragile, as confirmed by rheology measurements. The concentrated dispersions exhibit shear-thinning behavior at the shear rate 10^{-3} – 10^0 s^{-1} and Newtonian behavior on shearing (10^0 – 10^3 s^{-1}). Moreover, the viscosities of the LiMO dispersions are relatively higher than those of LEO dispersions at low shear rates. This work shows that it is possible to produce dispersions with a high volumetric energy density and controlled rheological properties by adjusting the percentage of solids.

AUTHOR INFORMATION

Corresponding Author

Yohanna Cabrera Orozco – Department of Geosciences and Natural Resource Management, University of Copenhagen, Frederiksberg C, Copenhagen 1958, Denmark; orcid.org/0000-0002-0388-496X; Email: yco@ign.ku.dk

Authors

Saket Kumar – Food Science Department, University of Copenhagen, Frederiksberg, Copenhagen 1958, Denmark
 Jens Risbo – Food Science Department, University of Copenhagen, Frederiksberg, Copenhagen 1958, Denmark
 Jacob Judas Kain Kirkenngaard – Food Science Department, University of Copenhagen, Frederiksberg, Copenhagen 1958, Denmark; Niels Bohr Institute, University of Copenhagen, Copenhagen Ø, Copenhagen 2100, Denmark; orcid.org/0000-0001-6265-0314

Complete contact information is available at:

<https://pubs.acs.org/10.1021/acssuschemeng.2c04017>

Notes

The authors declare no competing financial interest.

ACKNOWLEDGMENTS

The authors would like to thank the Danish Energy Agency for funding this work through the Energy Technology Development and Demonstration Program (EUDP), project “CLEO, a carbon-neutral fuel for the maritime sector”. The SAXS data were generated via a research infrastructure at the University of Copenhagen, partly funded by FOODHAY (Food and Health Open Innovation Laboratory, Danish Roadmap for Research Infrastructure). Y.C.O. is also grateful for the funding provided by A.P. Moller Maersk, project “LEO: Development and characterization of lignin biofuels for the marine shipping industry”, and the continuous support from their Head of Future Fuel, Maria Strandesen, and her team. Likewise, helpful academic discussions were held with Dr. Andrés Cabrera Orozco and Dr. Claus Felby. Technician Nanna Jacobsen helped with sample preparation, and Dr. Crispin Hetherington supported cryo-TEM imaging at Lund University.

REFERENCES

- (1) Chandra, R.; Yadav, S.; Kumar, V. Microbial Degradation of Lignocellulosic Waste and Its Metabolic Products. *Environ. Waste Manag.* **2015**, *249*–298.
- (2) Beauchet, R.; Monteil-Rivera, F.; Lavoie, J. M. Conversion of Lignin to Aromatic-Based Chemicals (L-Chems) and Biofuels (L-Fuels). *Bioresour. Technol.* **2012**, *121*, 328–334.
- (3) Vanholme, R.; Demedts, B.; Morreel, K.; Ralph, J.; Boerjan, W. Lignin Biosynthesis and Structure. *Plant Physiol.* **2010**, *153*, 895–905.
- (4) Abu-Omar, M. M.; Barta, K.; Beckham, G. T.; Luterbacher, J. S.; Ralph, J.; Rinaldi, R.; Román-Leshkov, Y.; Samec, J. S.; Sels, B. F.; Wang, F. Guidelines for Performing Lignin-First Biorefining. *Energy Environ. Sci.* **2021**, *14*, 262–292.
- (5) Renders, T.; Van den Bossche, G. V. d.; Vangeel, T.; Van Aelst, K. V.; Sels, B. Reductive Catalytic Fractionation: State of the Art of the Lignin-First Biorefinery. *Curr. Opin. Biotechnol.* **2019**, *56*, 193–201.
- (6) Kouris, P. D.; van Osch, D. J. G. P. van; Cremers, G. J. W.; Boot, M. D.; Hensen, E. J. M. Mild Thermolytic Solvolysis of Technical Lignins in Polar Organic Solvents to a Crude Lignin Oil. *Sustain. Energy Fuels* **2020**, *4*, 6212–6226.
- (7) Felby, C.; Mayer, S.; Cabrera, Y.. A Biofuel Composition Comprising Lignin. WO 2019158752 A1, 2019.
- (8) Cabrera, Y. Lignin Composition. WO 2022117391 A1, 2022.
- (9) Cabrera, Y.; Cabrera, A.; Jensen, A.; Felby, C. Purification of Biorefinery Lignin with Alcohols. *J. Wood Chem. Technol.* **2016**, *36*, 339–352.
- (10) Imel, A. E.; Naskar, A. K.; Dadmun, M. D. Understanding the Impact of Poly(Ethylene Oxide) on the Assembly of Lignin in Solution toward Improved Carbon Fiber Production. *ACS Appl. Mater. Interfaces* **2016**, *8*, 3200–3207.
- (11) Ratnaweera, D. R.; Saha, D.; Pingali, S. V.; Labbé, N.; Naskar, A. K.; Dadmun, M. The Impact of Lignin Source on Its Self-Assembly in Solution. *RSC Adv.* **2015**, *5*, 67258–67266.
- (12) Yang, M.; Zhao, W.; Singh, S.; Simmons, B.; Cheng, G. On the Solution Structure of Kraft Lignin in Ethylene Glycol and Its Implication for Nanoparticle Preparation. *Nanoscale Adv* **2019**, *1*, 299–304.
- (13) Zhao, W.; Xiao, L. P.; Song, G.; Sun, R. C.; He, L.; Singh, S.; Simmons, B. A.; Cheng, G. From Lignin Subunits to Aggregates: Insights into Lignin Solubilization. *Green Chem.* **2017**, *19*, 3272–3281.
- (14) Cheng, G.; Kent, M. S.; He, L.; Varanasi, P.; Dibble, D.; Arora, R.; Deng, K.; Hong, K.; Melnichenko, Y. B.; Simmons, B. A.; Singh, S. Effect of Ionic Liquid Treatment on the Structures of Lignins in Solutions: Molecular Subunits Released from Lignin. *Langmuir* **2012**, *28*, 11850–11857.
- (15) Savitskaya, T.; Reznikov, I.; Grinshpan, D. Rheological Behavior of Lignin Based Dispersions Intended for Composite Fuel Production. *Appl. Rheol.* **2016**, *26*, 1–7.
- (16) Burger, V. M.; Arenas, D. J.; Stultz, C. M. A Structure-Free Method for Quantifying Conformational Flexibility in Proteins. *Sci. Rep.* **2016**, *6*, 29040.
- (17) Huglin, M. B. *Light Scattering from Polymer Solutions*; Academic Press Inc.: London, 1972.
- (18) Sitar, S.; Aseyev, V.; Kogej, K. Microgel-like Aggregates of Isotactic and Atactic Poly (Methacrylic Acid) Chains in Aqueous Alkali Chloride Solutions as Evidenced by Light Scattering. *Soft Matter* **2014**, *10*, 7712–7722.
- (19) mono_gauss_coil — SasView 5.0.5 Documentation, 2022. (accessed SEP 09, 2022). https://www.sasview.org/docs/user/models/mono_gauss_coil.html.
- (20) Zimm, B. H. The Scattering of Light and the Radial Distribution Function of High Polymer Solutions. *J. Chem. Phys.* **1948**, *16*, 1093–1099.
- (21) Chakraborty, S.; Ding, J.; Thies, M. C.; Kitchens, C. L. More Elongated Solution Structures in Lignin Precursors Improve Properties of Resultant Carbon Fibers. *ACS Appl. Polym. Mater.* **2019**, *1*, 2561–2565.
- (22) Hu, T. Q. *Chemical Modification, Properties, and Usage of Lignin*; Springer, 2002.
- (23) powerLaw — SasView 5.0.5 Documentation, 2022. (accessed SEP 05, 2022). <https://www.sasview.org/docs/user/models/powerLaw.html>.
- (24) Mewis, J.; Wagner, N. J. Introduction to Colloid Science and Rheology. In *Colloidal Suspension Rheology*; Cambridge University Press: Cambridge, 2011; pp 1–35.
- (25) Hiemenz, P. C.; Rajagopalan, R. *Principles of Colloid and Surface Chemistry, Revised and Expanded*; CRC press, 2016.